Supporting Information

Electrocatalytic Reduction of Nitrite to Ammonium Ion Using Ni(II) Complexes with Redox-Active Di(imino)pyridine Ligands.

Somayeh Norouzinyanlakvan, Jeffrey Ovens, Darrin Richeson

Department of Chemistry and Biomolecular Sciences

University of Ottawa

Ottawa, ON Canada K1N 6N5

EXPERIMENTAL:

General: Reagents and analytical-grade solvents used in the synthesis were purchased from Sigma Aldrich and used without further purification. Doubly deionized water was used as a solvent in all reactions and procedures with a resistivity of 18.2 MΩ. For the indophenol test, ammonium sulfate and sodium citrate dihydrate were obtained from Fisher Scientific, phenol from Acros Organics, and sodium nitroferricyanide (III) dihydrate from Sigma-Aldrich. 3-(N-morpholino)propanesulfonic acid (MOPS) and sodium nitrite were obtained from Sigma-Aldrich. The nitrous oxide standard used in the GC-TCD studies was of AA grade and obtained from Air Products. Compound **1** was prepared and characterized as previously reported.[1]

X-ray Crystallography: The crystals of $NiBr_2$-2,6-Bis{1-[(2,6-diisopropylphenyl)imino]-benzyl}pyridine (**2**) were mounted on thin glass fibers using paraffin oil. Prior to data collection crystals were cooled to 200.15 °K. Data were collected on a Bruker Smart Apex II single crystal diffractometer equipped with a sealed tube Mo source (wavelength 0.71073 Å) and a CCD detector. Raw data collection and processing were performed with the Apex3 software package from Bruker.[2] Initial unit cell parameters were determined from 60 data frames from select ω scans collected at the different sections of the Ewald sphere. Semi-empirical absorption corrections based on equivalent reflections were applied.[3] Systematic absences in the diffraction data set and unit-cell parameters were consistent with the assigned space group. The initial structural solution was determined using ShelxT direct methods,[4] and refined with full-matrix least-squares procedures based on F^2 using ShelXle.[5] Hydrogen atoms were placed geometrically and refined using a riding model. All scattering factors are contained in several versions of the ShelXL program library, with the latest version used being v.6.12 at the time of this writing.

Electrochemistry: Electrochemical experiments were carried out in a single compartment cell, with 40 mL approximate volumes, using a VersaSTAT 3 (Princeton Applied Research) potentiostat. Samples were prepared in an open air, sealed, and connected to a Schlenk line and maintained under a nitrogen atmosphere. A conventional three electrode system was employed consisting of a glassy carbon working electrode (diameter = 0.3 cm), a Pt wire as the auxiliary electrode, and an Ag wire as a pseudo-reference electrode. Ferrocene was added as a reference compound and potentials were referred to the redox potential of ferrocenium ion (Fc^+)/ferrocene (Fc) as an internal standard. Dried acetonitrile was purchased from Sigma Aldrich and stored on molecular sieves in the glovebox. Tetrabutylammoniumhexafluorophosphate, $[(n\text{-}Bu)_4N]PF_6$ (TBAHFP), the supporting electrolyte, was crystallized two times with ethanol, dried under vacuum at 90 °C for 24 h before used and stored in a glovebox. Deionized (DI) water was used. The typical concentration of catalyst was 1 mM in each experiment. All the background experiments were performed in sealed 40-mL three neck cell.

Other Physical Measurements: Gas chromatography (GC) for detection of gas products was conducted on a Shimadzu GC- 2014 equipped with a thermal conductivity detector (TCD). Helium carrier gas (purity ≥ 99.995%) was utilized with an isothermal 6-minute run at 30 ºC on an Agilent HP-PLOT Q column. UV-vis spectra were recorded with a Cary 100 spectrophotometer. The ^1H NMR spectra were recorded at 162 MHz respectively with chemical shifts reported in ppm using the residual protons of the NMR solvent as internal standards. Mass spectrometric measurements were performed at the Chemistry Mass Spectrometry Facility at the University of Ottawa, Ontario on a Micromass Quattro triple quadrapole mass spectrometer equipped with an electrospray ionization source. ^{14}N nuclear magnetic resonance spectroscopy (NMR) was carried out using a Bruker Avance 500 instrument operating at 36.1 MHz for the ^1H nucleus and the ^{14}N nucleus. Nitromethane ($MeNO_2$) was used as an external standard. For each sample, 500 scans were obtained with a relaxation delay (d1) of 10 seconds to allow for sufficient relaxation of $^{14}NH_4^+$ nuclei. Quantification of NH_4^+ is performed via addition of a capillary tube containing

1.0 M $MeNO_2$ to the NMR tube where indicated. A calibration curve was made by comparing the peak areas of standards with known [NH_4^+] compared to the peak area of the 1.0 M $MeNO_2$ standard within the capillary tube (Figure S16).

Myoglobin Test for NO

Flowing N_2 gas was utilized to bubble the headspace of the controlled potential coulometry (CPC) cell after overnight electrolysis (1mM $NiLBr_2$, 40mM MOPS, 50mM $NaNO_2$, at –1.4 V) through a solution containing 500 µM Fe(II) myoglobin (Mb(II)) in 100 mM phosphate buffer at pH 7.4. Following CPC, a 50x dilution of the Mb(II) solution was then assessed by absorption spectroscopy .[6]

Indophenol blue test:[7]

1mL of reagent A (100 mL aqueous solution of 11.1ml liquefied phenol in ethyl alcohol) and 25mL of sample solution are added into a test tube. After the tube is vigorously shaken, 1 mL of reagent B (0.5% w/v nitroprusside aqueous solution) is added into the test tube and is shaken. 2.5ml of reagent D (12.5ml of 5% sodium hypochlorite in 50ml reagent C (50g trisodium citrate plus 2.5g sodium hydroxide in 250 water)) is added to the test tube and vigorously shaken. This solution is moved to a 50ml volumetric flask, and the volume is filled with water. The color of the solution is developed at room temperature for 1 hour and the absorbance at 640 nm was measured at room temperature. A calibration curve for ammonia quantification is constructed using standard ammonium chloride solution (Figure S14). The amount of ammonium after electrolysis is quantified according to this calibration curve. Control experiments reveal that color development does not occur in the presence of any of the species present in the electrocatalysis experiments, i.e. catalyst, electrolyte, etc.

Spectroscopic test to measure hydroxyl amine:[8]

1ml of reagent A (0.96ml of 1M sodium acetate solution in 1.14ml of 1M acetic acid solution) is added to 25ml of sample in a test tube and is vigorously shaken. 1ml of Reagent B (0.0192gr of ferric ammonium sulfate in 10ml 0.1M HCl) is added to the test tube and is shaken. 1ml of reagent C (0.018gr of 1,10 phenanthroline in 10ml 1M acetic acid solution) and shaken again. The color of the solution is developed at room temperature for 30 minutes and the absorbance at 510 nm measured at room temperature. A calibration curve for hydroxylamine quantification is constructed using standard hydroxylamine solution. The amount of NH_2OH after electrolysis is quantified according to this calibration curve (Figure S15). Control experiments reveal that color development does not occur in the presence of any of the species present in the electrocatalysis experiments, i.e. catalyst, electrolyte, etc.

Equations:

Faradaic efficiency (FE) was calculated from the following equation:

$$FE\ (\%) = (ne \times F \times 100\%) / QT$$

Where ne = the moles of electrons required to generate the measured moles of a species of interest from NO_2^- (6 moles of electrons per mole of ammonium, 4 moles of electrons per mole of hydroxylamine, F = Faraday's constant (96485.3 C/mol e-), and QT = the total charge passed during the CPC experiment in coulombs.

Randles-Sevcik equation:

$i_p = 0.496(FAC)(DFv/RT)^{1/2}$

The Randles-Sevcik equation which describes the peak current of a mass-transport limited event establishes a relationship of peak current being proportional to the square root of the scan rate. In the Randles-Sevick equation, i_p describes peak current observed in CV, F is the Faraday constant, A is the surface area of the electrode in cm^2, C is the concentration of electroactive species in mol/cm^3, D is the diffusion coefficient of the electroactive species in cm^2/s, v is the scan rate in V/s, R is the ideal gas constant, and T is the absolute temperature.

Synthesis of *2,6-Bis{[2,6-di(isopropyl)phenyl)imino]benzyl}pyridine*:
A mixture of 2,6-dibenzoylpyridine (5.0 g, 17.4 mmol), 2,6 diisopropylaniline (3.5 g, 17.4 mmol), and p-toluene sulfonic acid (0.2 mg) in toluene (50 mL) were placed in a round bottom flask equipped with a Dean–Stark trap. Under a nitrogen atmosphere, the reaction mixture was heated to reflux in an oil bath at 140˚C for 48 h then cooled to room temperature and the solvent was removed under vacuum to give a dark yellow oil. Hexanes were added and a small quantity of a white solid was removed by filtration. The filtrate was removed under vacuum yielding a dark yellow oil. Methanol (~400 mL) was added to this oil and the mixture was stirred for several minutes, causing the product to precipitate as a yellow solid which was filtered off and rinsed with methanol. The filtrate was reduced to about half the initial volume under vacuum, and then placed in a refrigerator, causing additional product to precipitate, which was filtered and rinsed with methanol. The product was obtained as a yellow powder. Yield: 7.2 g (68%). ^{1}H NMR (T = 115˚C, d6-dimethyl sulfoxide, 162 MHz) δ 7.82 (br t, 1 H, py, p CH), 7.55–7.20 (br m, 12 H, Ar–H), 6.94 (br s, 6H, Ar–H), 2.90 (m, 4H, iPr), 1.00 (d, 24H, iPr) ppm.

Synthesis of *$NiBr_2$-2, 6-Bis{1-[(2,6-diisopropylphenyl)imino]-benzyl}pyridine* (2):
$NiBr_2$ powder (34 mg, 0.160 mmol) was added to a clear yellow solution of ligand **L2** (100 mg, 0.165 mmol) in 6 mL of toluene. The reaction mixture was allowed to stir for 4 hours, gradually becoming brown. The solution was then held at -20^{o}C overnight, over which time a light brown precipitate formed. The precipitate was removed by filtration and washed with 5 x 2 mL hexanes, and allowed to dry under vacuum. A light brown powder was isolated in 78% yield. Brown needle-like crystals suitable for X-ray analysis were grown from saturated dichloromethane solution by diffusion of hexane and storing at -20^{o}C for several hours. ^{1}H NMR (T = 115˚C, d-chloroform, 162 MHz) δ 8.46 (d, 2 H, py, m CH), 7.91 (t, 1 H, py, p CH), 7.18-7.03 (br m, 16H, Ar–H), 2.75 (m, 4H, iPr), 1.14 (d, 24H, iPr) ppm. Elemental analysis calculated for $C_{43}H_{47}Br_2N_3Ni$: C, 62.65; H, 5.75 N, 5.10. Found: C, 62.87; H, 6.05 N, 4.94.

Computational Details: Optimized structures were obtained from density functional theory (DFT) computations using the Gaussian 09 package.[9] The B3LYP functional and def2TZVP basis set was used for all atoms. The initial optimizations began with the experimental X-ray structure as input. Optimizations for the subsequent reduction steps to generate anions began with the optimized structure from the preceding species. All optimizations used the PCM model for solvation with acetonitrile as the solvent. Frequency analysis confirmed that the optimized structures were minima with no imaginary frequencies.

The canonical molecular orbitals and fragment orbital compositions were generated using the Chemissian program.

Table S1. Crystal data and structure refinement for **(2)**

Compound	
Empirical formula	$C_{44}H_{49}Br_2Cl_2NiN_3$
Formula weight	909.29
Temperature(K)	203(2)
λ (Å)	0.71073
Crystal system	Triclinic
Space group	P -1
a (Å)	9.5290(6)
b (Å)	9.7708(6)
c (Å)	13.6707(9)
α (deg)	93.325(2)
β (deg)	107.464(2)
γ (deg)	114.272(2)
V (Å3)	1082.49(12)
Z	1
p (calc) (Mg/m3)	1.395
Mu (mm-1)	2.450
R1a	0.0296
wR2b	0.0749

Table S2. Selected Bond lengths [Å] and angles [°] for (**2**)

Bond lengths [Å]		**Bond angles [°]**	
Br(1)-Ni(1)	2.451 (2)	N(1)-Ni(1)-N(2)	77.2(5)
Ni(1)-N(1)	1.99(1)	N(1)-Ni(1)-N(3)	76.9(4)
Ni(1)-N(2)	2.17(1)	N(2)-Ni(1)-N(3)	151.2(4)
N1(i)-N(3)	2.20(1)	Br(2)-Ni(1)-Br(1)	118.75(8)
Ni(1)-Br(2)	2.348(2)	C(7)-N(2)-Ni(1)	114.1(9)
N(1)-C(1)	1.34(2)	C(20)-N(2)-Ni(1)	126.1(9)
N(2)-C(7)	1.29(2)	C(21)-N(3)-Ni(1)	127.1(9)
N(2)-C(20)	1.45(2)	C(5)-N(1)-Ni(1)	117.4(9)
N(3)-C(6)	1.28(2)	C(1)-N(1)-Ni(1)	117.4(9)
N(3)-C(21)	1.46(2)	Br(1)-Ni(1)-N(2)	95.2(3)
C(5)-N(1)	1.32(2)	Br(2)-Ni(1)-N(2)	97.7(3)

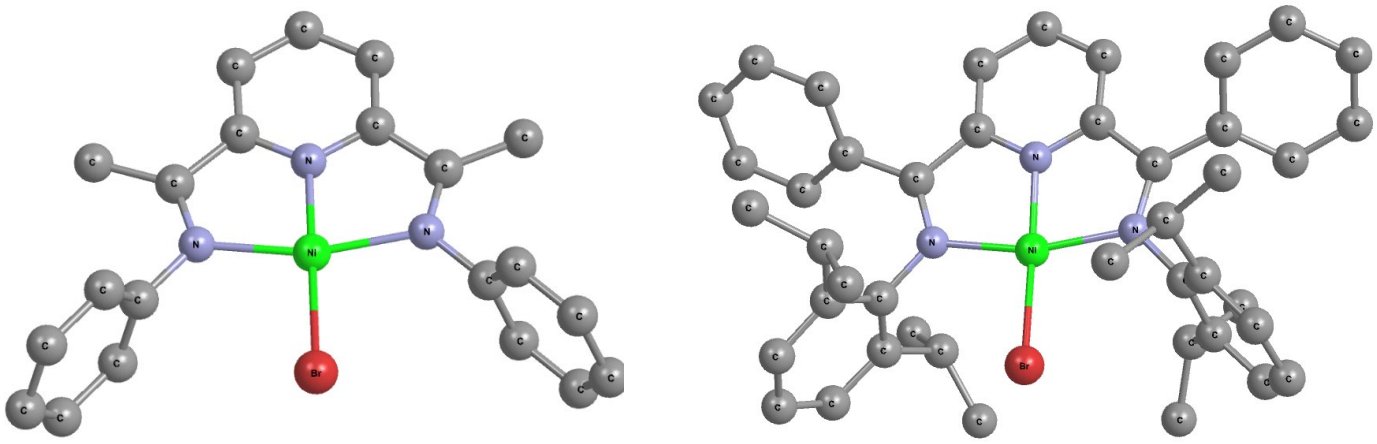

1'$^{+}$ **2'**$^{+}$

Figure S1. Computationally optimized [Ni(κ^3-2,6-{PhN=CMe}$_2$(NC_5H_3)Br]$^+$ (**1'**$^+$) and [Ni{κ^3-2,6-[(^{i}Pr$_2$$C_6H_3$)N=CPh]$_2$($NC_5H_3$)Br]$^+$ (**2'**$^+$) (DFT, B3LYP, def2-TZVP) using the PCM model for solvation in acetonitrile. Hydrogen atoms have been omitted for clarity.

Table S3. Selected bonding parameters for computationally optimized [Ni(κ^3-2,6-{PhNCMe}$_2$(NC_5H_3)Br]$^+$ (**1'**$^+$) and Ni{κ^3-2,6-[(^{i}Pr$_2$$C_6H_3$)N=CPh]$_2$($NC_5H_3$)Br]$^+$ (**2'**$^+$).

Compound **1'**$^+$			
Bond	Length(Å)	Overlap Pop	Mayer Bond Order
Ni-N_{imine}	1.976	0.265	0.654
Ni-N_{py}	1.847	0.209	0.681
Ni-Br	2.339	0.344	1.00
Compound **2'**$^+$			
Bond	Length(Å)	Overlap Pop	Mayer Bond Order
Ni-N_{imine}	1.991	0. 297	0.650
Ni-N_{imine}	1.992	0.293	0.648
Ni-N_{py}	1.847	0.251	0.724
Ni-Br	2.339	0.280	0.813

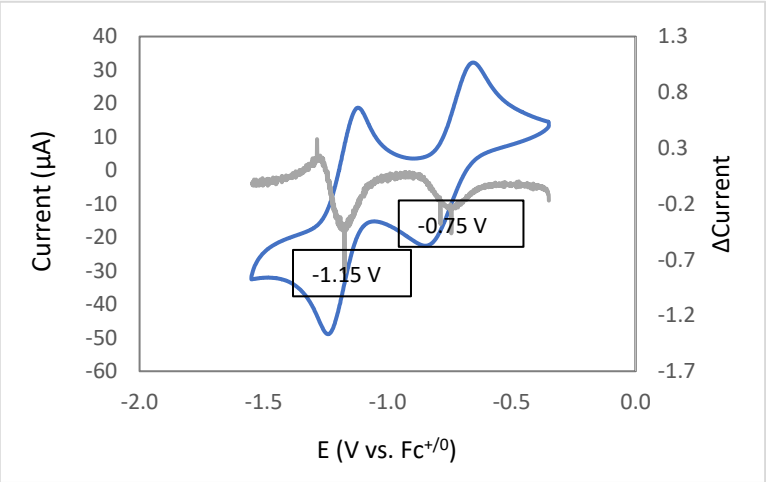

Figure S2. Cyclic voltammogram of $[Ni(\kappa^3\text{-}2,6\text{-}\{PhNCMe\}_2(NC_5H_3)Br]^+$ (**1**) (1mM) in CH_3CN with 100mM TBAHFP using a glassy carbon (GC) working electrode. Potentials are referenced to $Fc^{0/+}$. Two reversible reduction peaks were observed with $E_{1/2}$ of -0.75 V and -1.15 V. The gray markers represent application of the method of first principles to the blue curve. Minima denote inflection points in the catalytic curve and indicate the associated onset potential and current enhancement.

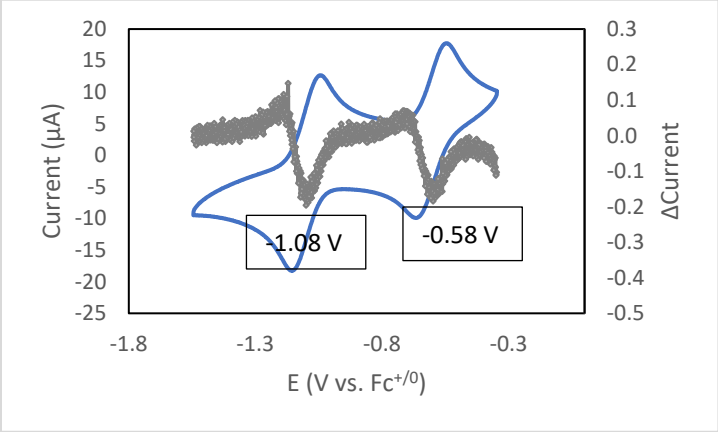

Figure S3. Cyclic voltammogram of $[Ni(\kappa^3\text{-}2,6\text{-}\{2,6\text{-}^iPr_2C_6H_3NCMe\}_2(NC_5H_3)Br]^+$ (**2**) (1mM) in CH_3CN with 100mM TBAHFP using a glassy carbon (GC) working electrode. Potentials are referenced to $Fc^{0/+}$. Two reversible reduction peaks were observed with $E_{1/2}$ of -0.58 V and -1.08 V. The gray markers represent application of the method of first principles to the blue curve. Minima denote inflection points in the catalytic curve and indicate the associated onset potential and current enhancement.

a

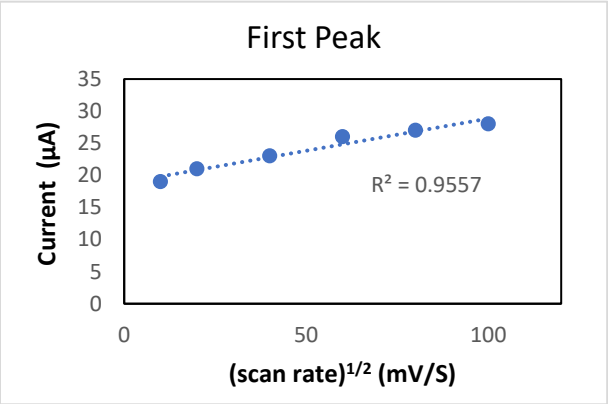

b

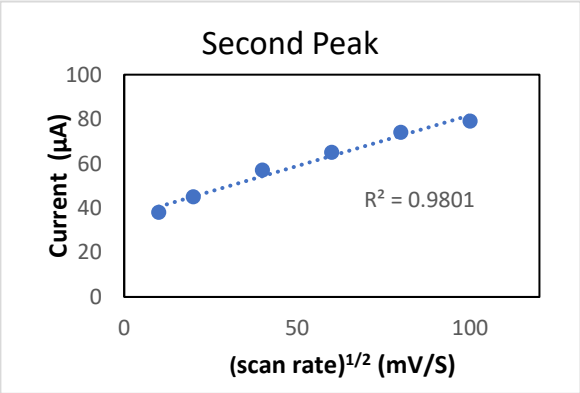

Figure S4. Plots of scan rate$^{1/2}$ versus current for the (a) first at -0.58V, (b) second at -1.08 V, reduction peaks of (**2**).

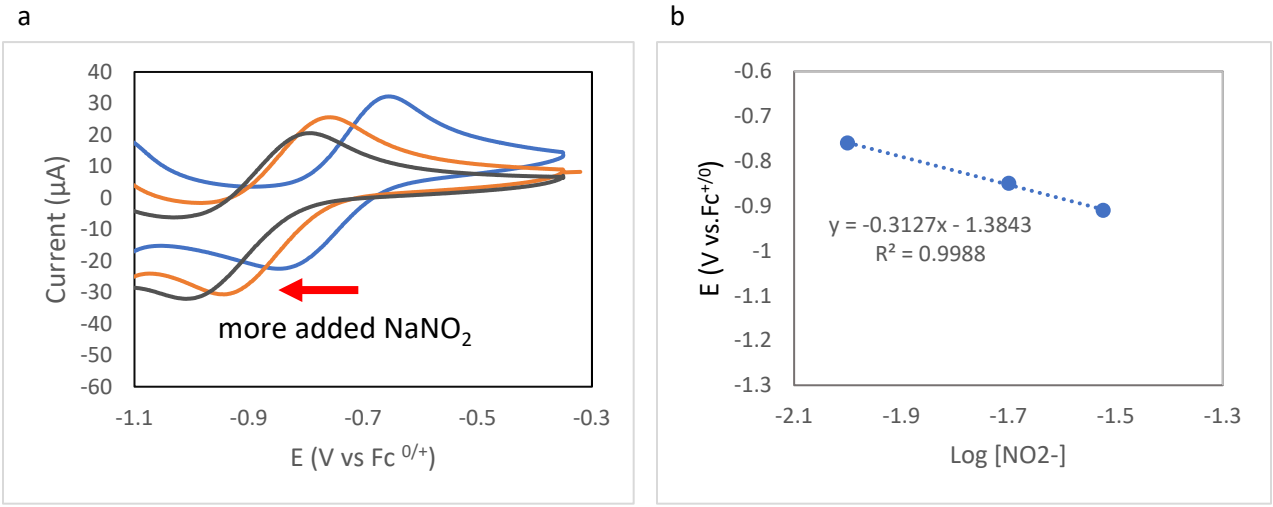

Figure S5. (a) Selected cyclic voltammograms of 1 mM **1** with different concentrations of $NaNO_2$ (scan rate = 100 mV/s, glassy carbon working electrode (b) Plot of E vs log[NO_2^-], where E values are calculated from cyclic voltammograms and [NO_2^-] is the concentration of $NaNO_2$ in solution.

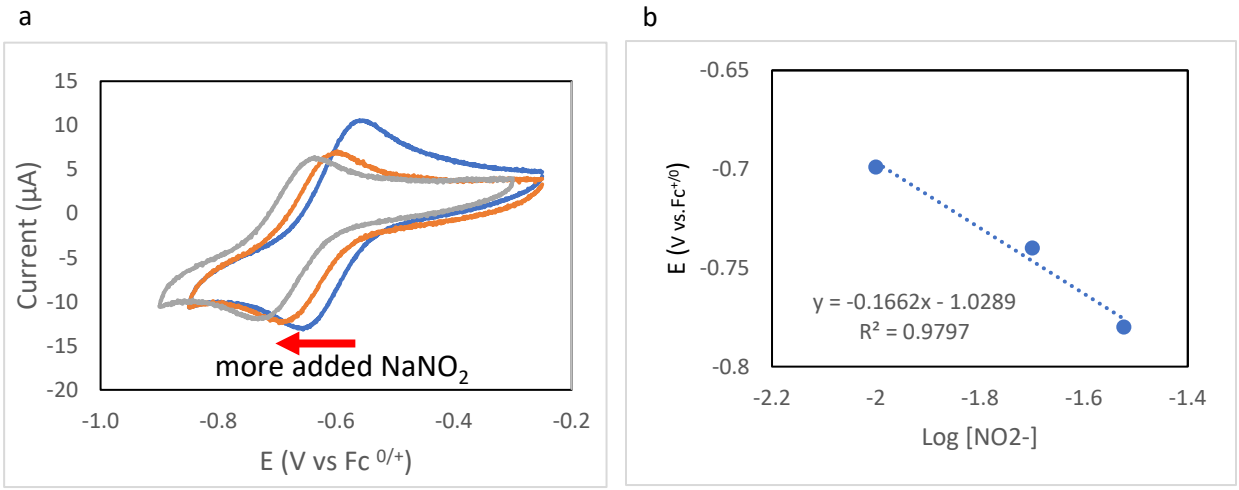

Figure S6. (a) Selected cyclic voltammograms of 1 mM **2** with different concentrations of $NaNO_2$ (scan rate = 100 mV/s, glassy carbon working electrode (b) Plot of E vs log[NO_2^-], where E values are calculated from cyclic voltammograms and [NO_2^-] is the concentration of $NaNO_2$ in solution.

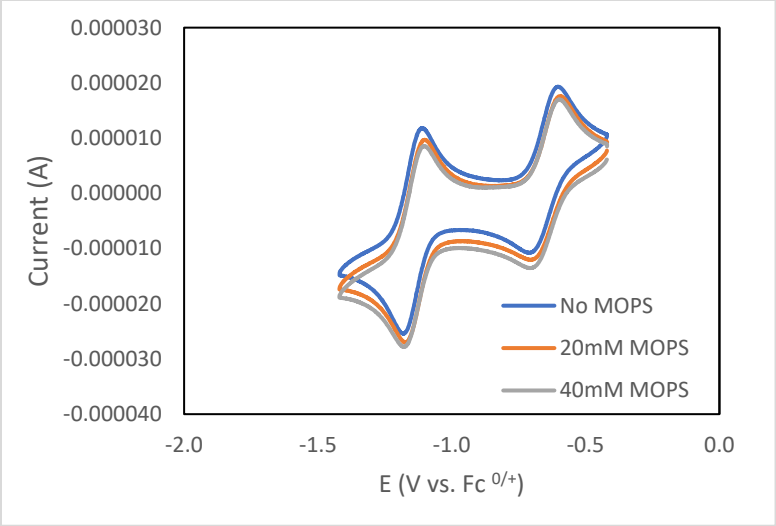

Figure S7. Selected cyclic voltammograms of 1 mM **1** with different concentrations of MOPS (scan rate = 100 mV/s, glassy carbon working electrode.

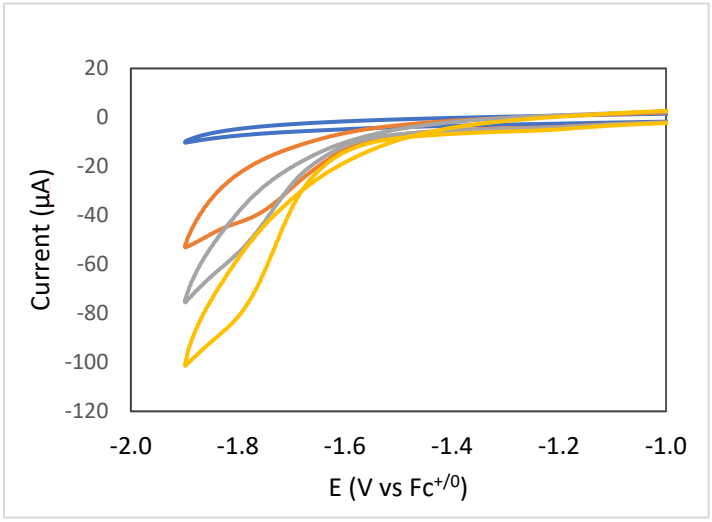

Figure S8. Selected cyclic voltammograms of (100 mV/s) of 0.1 M TBAHFP, 40 mM MOPS, with $NaNO_2$ titrated from 0 to 150mM, using a glassy carbon (GC) working electrode.

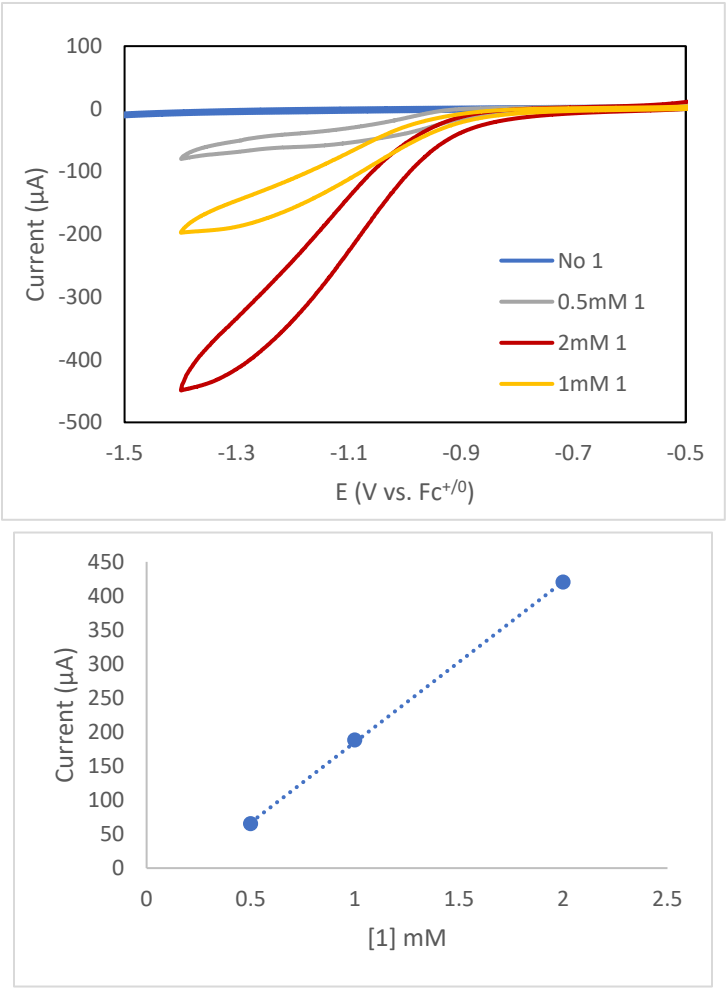

Figure S9. a) Cyclic voltammograms (100 mV/s) of 0.1 M TBAHFP, 40 mM MOPS, 50mM $NaNO_2$, with different concentrations of **1** in a mixture of CH_3CN/H_2O (50/50). b) Plot of peak current versus the concentration of **1** titrated.

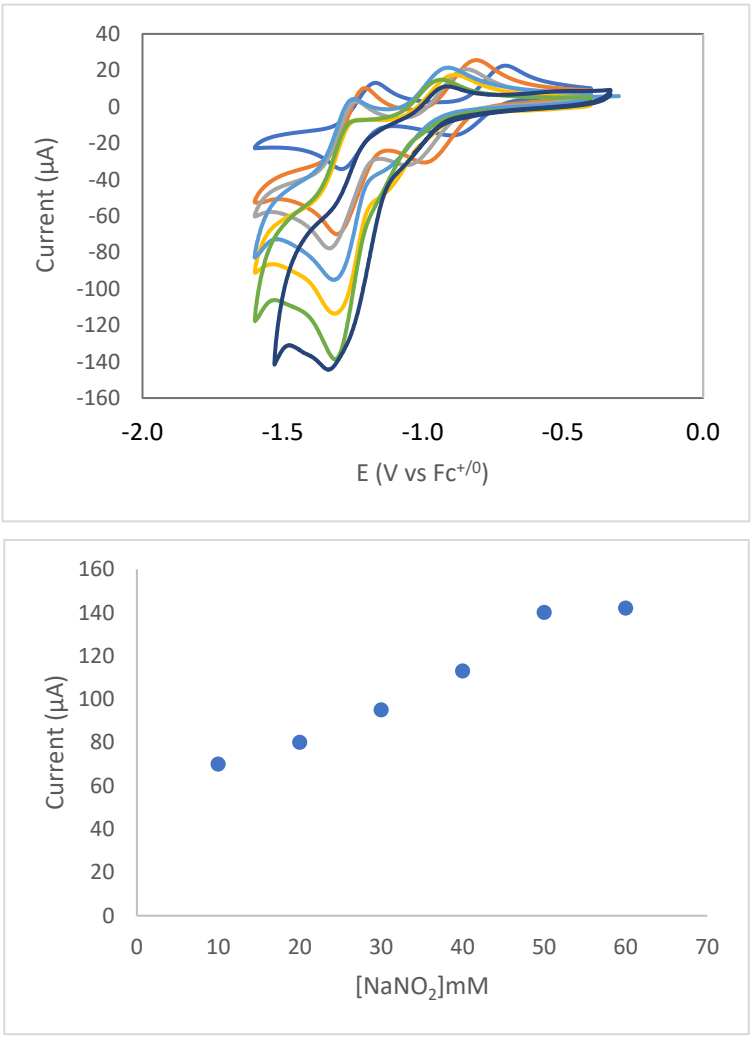

Figure S10. a) Cyclic voltammograms (100 mV/s) of 0.1 M TBAHFP, 40 mM MOPS, 1mM **1**, with NaNO2 titrated from 0 to 70 mM in increments of 10 mM initially, in a mixture of CH_3CN/H_2O (50/50). b) Plot of peak current versus the concentration of NaNO2 titrated.

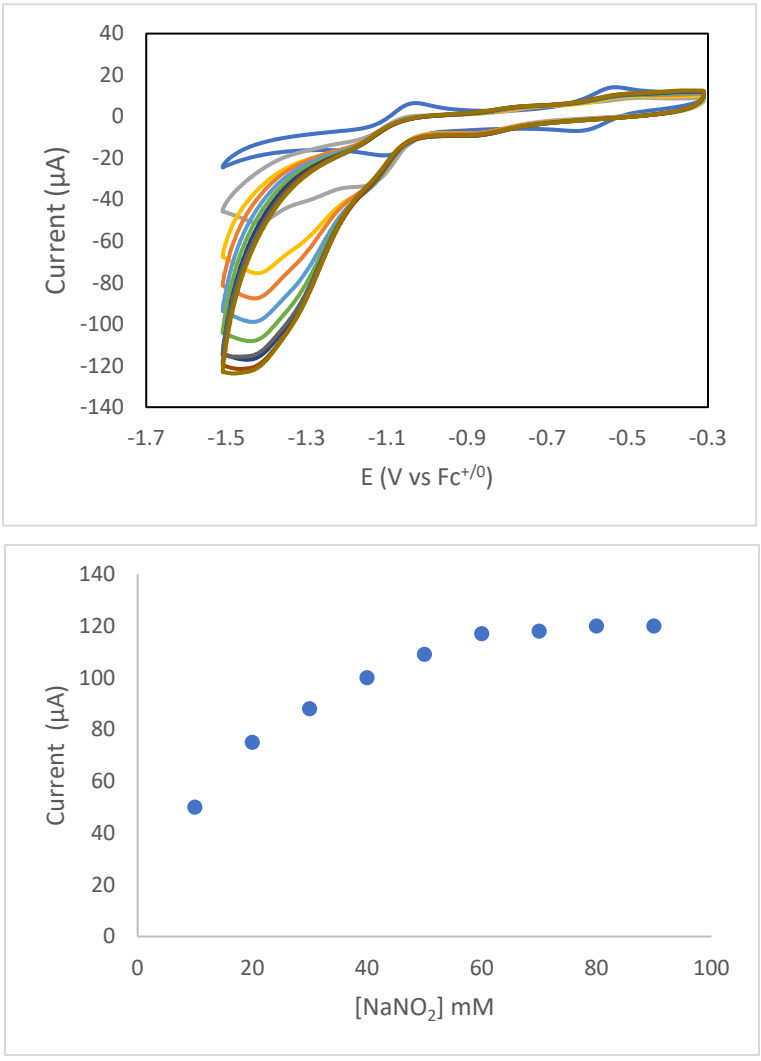

Figure S11. a) Cyclic voltammograms (100 mV/s) of 0.1 M TBAHFP, 40 mM MOPS, 1mM **2**, with $NaNO_2$ titrated from 0 to 90 mM in increments of 10 mM initially. b) Plot of peak current versus the concentration of $NaNO_2$ titrated.

Foot-Of-The-Wave Analysis of the Nitrite Reduction by Complexes **1** and **2:**

The foot-of-the-wave analysis (FOWA) allows for an estimate of the reaction rate for an electrocatalytic process that does not show the limiting S-curve behavior.[10,11] This analysis examines the data at the earliest points in the catalytic wave, before E_{cat}. The resulting curve is then fitted to a linear function within the region that the parent function remains linear and the slope of this line can be used to extract the k_{FOW} of the electrocatalytic reaction of interest. The k_{FOW} is often presented as turnover frequency (TOF). Strictly speaking, this TOF is the number of moles of product produced per unit time per mole of catalyst contained in the reaction−diffusion layer at the electrode and not relative to the catalyst molecules in the bulk solvent. Furthermore, TOF is only equal to k_{FOW} when the applied potential has converted all the catalyst molecules into the active reduced form.

Following the FOWA method described in the literature[10–13], the first step is to use the applied potential, E, and the potential where the catalyst undergoes the reduction process , E_{redox}, in the following relationship:

$$\exp\left[\frac{nF}{RT}(E - E_{redox})\right] \qquad \text{eqn. 1}$$

Where *R* is the universal gas constant, *T* is the temperature, *n* is the number of electrons transferred to the catalyst, and *F* is the Faraday constant. This relationship used in the FOWA relationship given by equation 2 using the ratio of the catalytic current (i_c) divided by the non-catalytic Faradaic peak current (i_p) of a reduction wave (E_{redox}):

$$i_c/i_p = 2.24\sqrt{\left(\frac{RT}{nFv}\right)(k_{FOW})}\,\frac{1}{1+\exp\left[\frac{nF}{RT}(E-E_{redox})\right]} \qquad \text{eqn. 2}$$

In this equation, ν is the scan rate in V/s. Taking the ratio of i_c to i_p simplifies the overall analysis by avoiding the determination of catalyst diffusion coefficient and electrode surface area.

With this approach a plot ic/ip versus $\frac{1}{1+\exp\left[\frac{nF}{RT}(E-E_{redox})\right]}$ at the "foot of the wave" allows for a linear extrapolation. The slope of this line, m, is given by equation 3.

$$m = 2.24\sqrt{(RT/nFv)(k_{FOW})} \qquad \text{eqn. 3}$$

and

$$k_{FOW} = 0.776\ (m)^2 \qquad \text{eqn. 4}$$

In this set of experiments we used n = 1, corresponding the second reduction of compounds **1** and **2**, as the first rate-determining chemical step. This leads to a lower limit to TOF.

For a general multielectron catalytic system, the number of unique electron-transfer processes that occur at the electrode per catalyst (n) and the catalyst equivalents used per turnover (n') are incorporated into eqs 2 and 3 , giving eqs 5 and 6.[13]

$$i_c/i_p = 2.24\sqrt{(RT/nFv)n'(k_{FOW})}\,\frac{1}{1+\exp\left[\frac{nF}{RT}(E-E_{redox})\right]} \qquad \text{eqn. 5}$$

$$m = 2.24\sqrt{(RT/nFv)n'(k_{FOW})} \qquad \text{eqn. 6}$$

In the case of nitrite reduction to ammonium ion, n'= 6 and eqn 6 reduces to:

$$k_{FOW} = 0.129(m)^2 \qquad \text{eqn. 7}$$

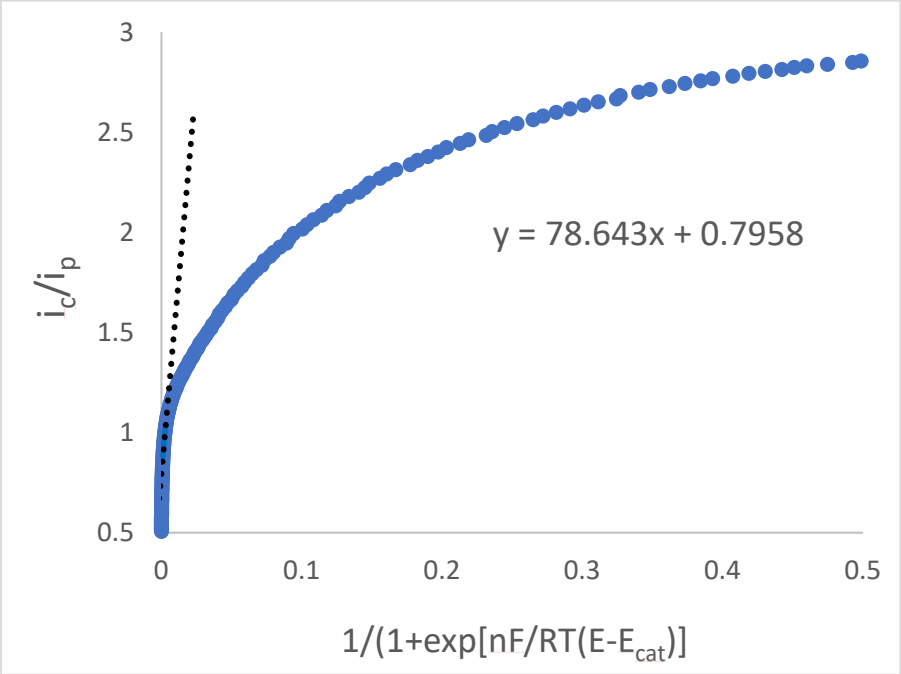

Figure S12. FOWA plot of i_{cat}/i_p versus $1/[1 + \exp\{(F/RT)(E - E_{redox})\}]$ for the nitrite electrocatalytic reduction with compound **1** in a MOPS buffered solution. The linear fit of the region of the FOWA analysis as E approaches E_{redox} is shown as a dotted line and the corresponding equation and the slope were used to calculate the k_{FOW}.

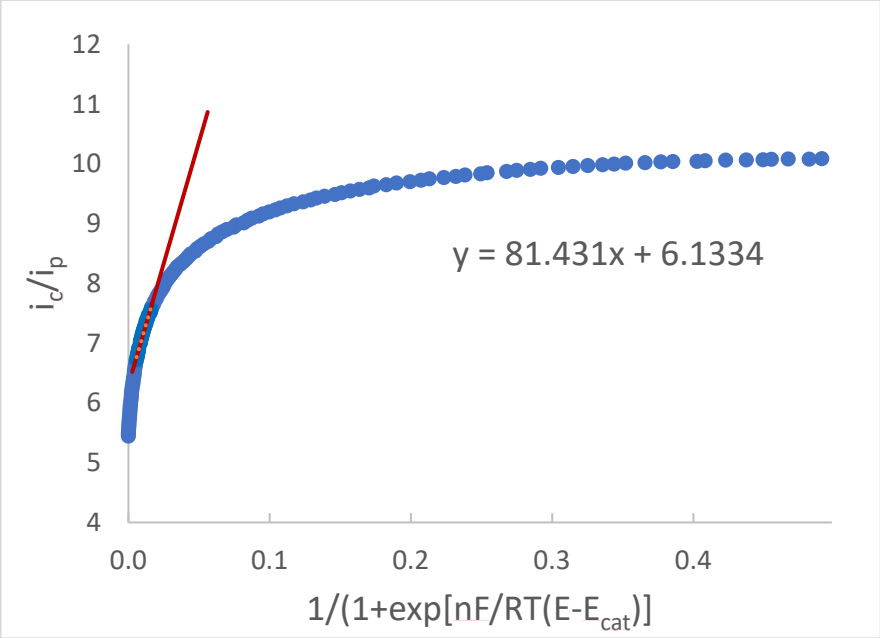

Figure S13. FOWA plot of i_{cat}/i_p versus $1/[1 + \exp\{(F/RT)(E - E_{redox})\}]$ for the nitrite electrocatalytic reduction with compound **2** in a MOPS buffered solution. The linear fit of the region of the FOWA analysis as E approaches E_{redox} is shown as a red line and the corresponding equation is given and the slope was used to calculate the k_{FOW}.

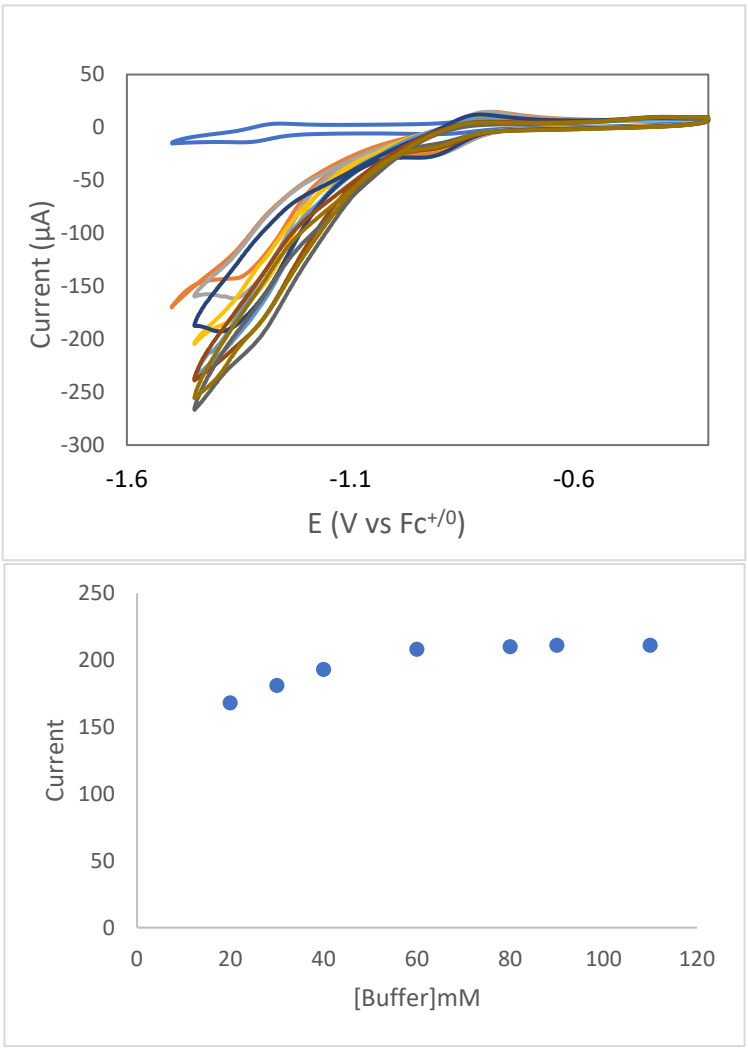

Figure S14. a) Cyclic voltammograms (100 mV/s) of 0.1 M TBAHFP, 50 mM NaNO2, 1mM **1**, with MOPS titrated from 0 to 110 mM in increments of 10 mM initially, in a mixture of CH_3CN/H_2O (50/50). b) Plot of peak current versus the concentration of MOPS titrated.

.

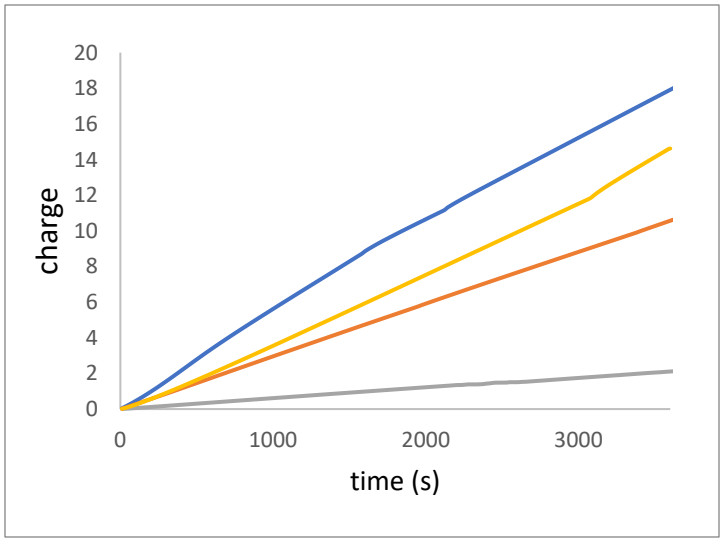

Figure S15. Controlled potential coulometry (CPC) at –1.4 V vs. $Fc^{+/0}$ (100 mV/s) **a**) of a solution containing 50mM $NaNO_2$ and 40 mM MOPS with different concentrations of **1**, 0mM (gray), 0.5mM(orange), 1mM(yellow), 2mM(blue) over 1 hour period CPC.

Table S4. Summary of 4-hour CPC experiment at -1.4V vs $Fc^{+/0}$ in a 50/50 acetonitrile/water solution. Unless otherwise noted experiments used 1mM catalyst (**1** or **2**) 40mM MOPS, and 50mM $NaNO_2$. The disproportionation experiments were carried out with 1mM of **1**, 40mM MOPS and the substrate indicated.

Exp.	Catalyst	Time (hour)	µmol of NH_4^+	µmol of NH_2OH	Total FE (%)	FE for NH_4^+(%)	FE for NH_2OH(%)	Charge	TON
1	**1**	4	50	9	54	48	6	60	2.94
2	**2**	4	75	0	50	50	-	89	4.41
	Background								
3	**No catalyst**	4	0	0		-	-	12	
4	1+**No MOPS**	4	0	0		-	-		
	Disproportionation								
5	1 + **100mM NH_2OH**	4	197	-	73	73	-	160	11.6
6	1+**N_2O**	4	0	0		-	-	14.39	
7	1+**NO**	4	0	0		-	-	13.04	

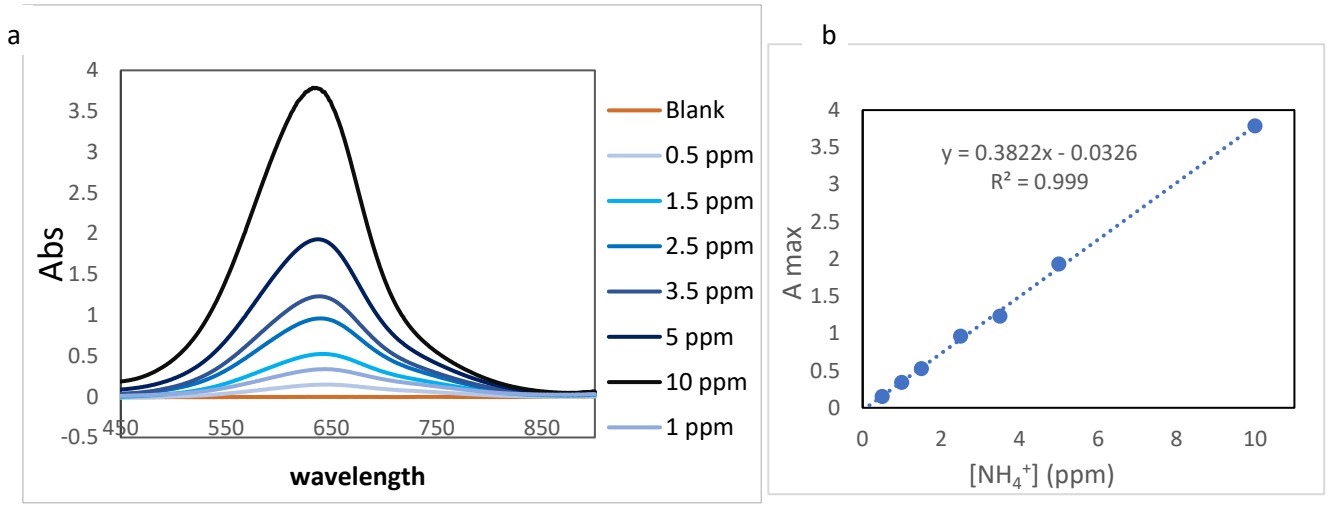

Figure S16. a) UV-vis spectra of the $(NH_4)_2SO_4$ standards for the indophenol blue test containing 0 to 10 µM ammonium. b) Calibration curve for the indophenol blue test.

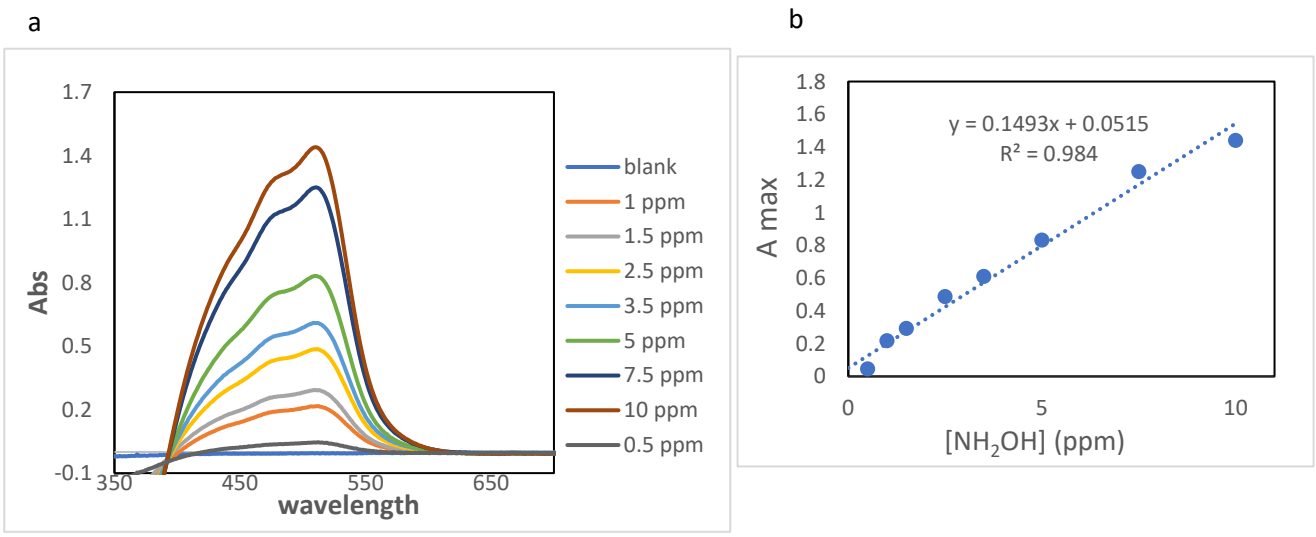

Figure S17. a) UV-vis spectra of the (NH_2OH) standards for the spectroscopic test to measure hydroxylamine containing 0 to 10 µM hydroxylamine. b) Calibration curve for the hydroxylamine test.

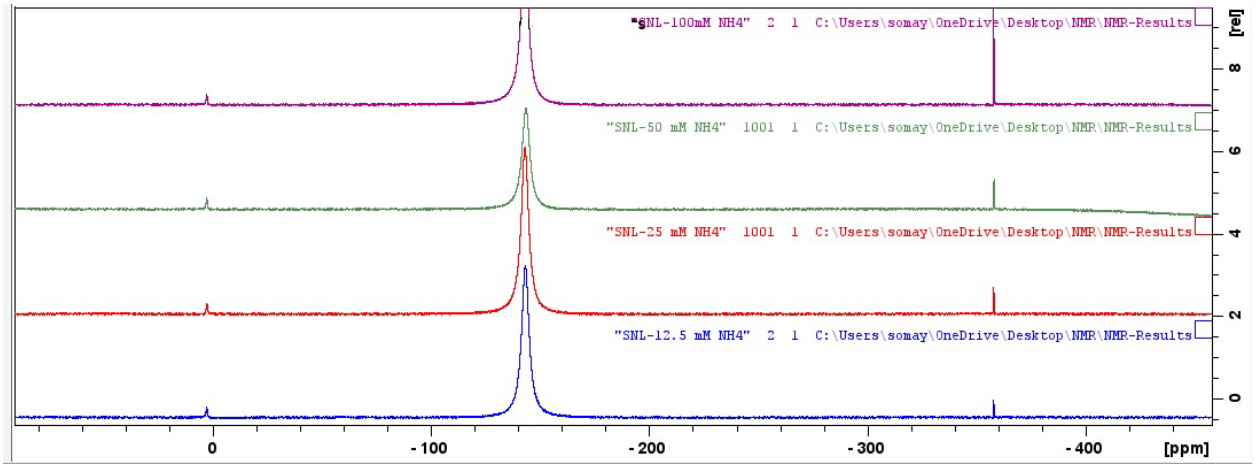

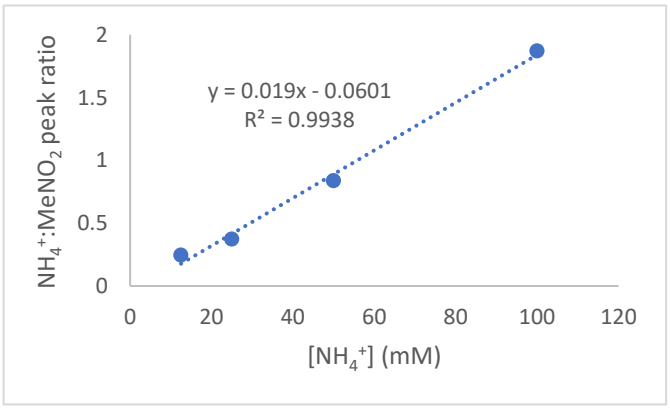

Figure S18. A) ^{14}N NMR of standards containing 12.5 to 100 mM NH_4^+ with capillary tubes containing 1.0 M $MeNO_2$. B) calibration curve made by plotting the ^{14}NNMR peak ratio of NH_4^+ to $MeNO_2$ for the NH_4^+ standards shown in a.

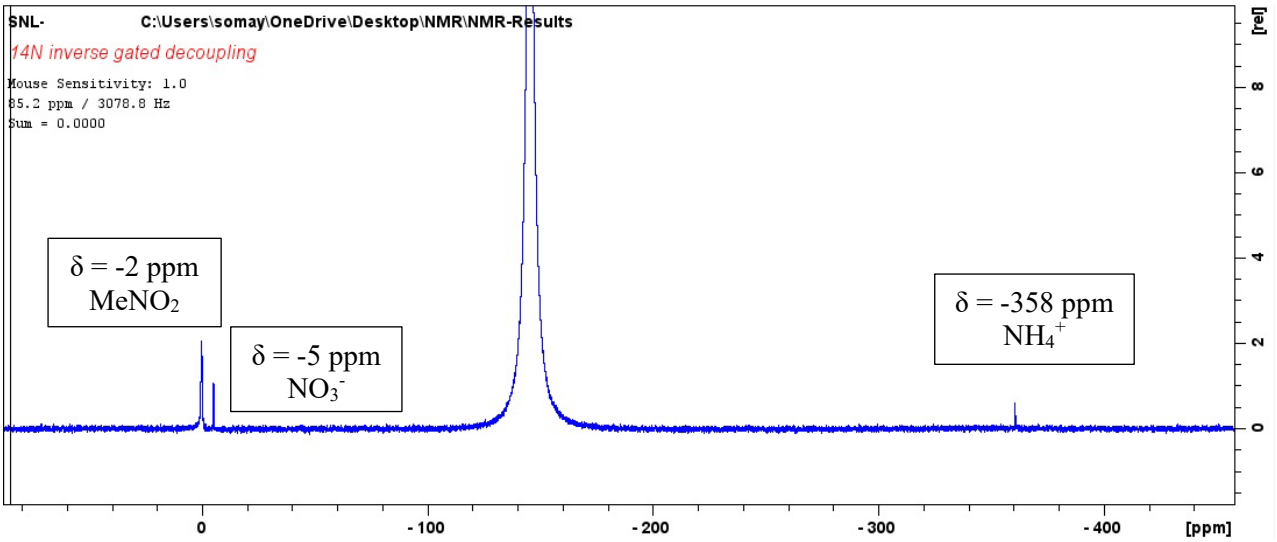

Figure S19. ^{14}N NMR (500 MHz) of aqueous solutions obtained following the CPC experiment shown in Table S4, row 1. The sharp peak observed at δ =-358 ppm is attributed to NH_4^+, the peak at δ =-2 attributed to $MeNO_2$, and the peak at δ =-5 attributed to NO_3^- as an oxidation product of nitrite.

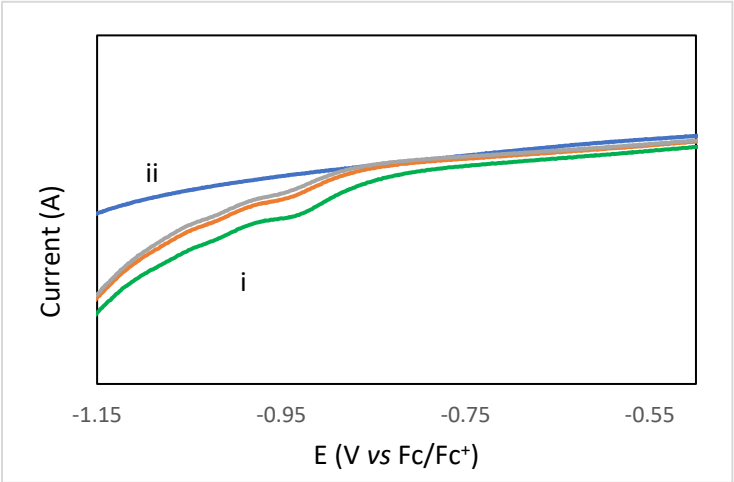

Figure S20. LSV measurements used to demonstrate that the working electrode surface remains clean during catalysis. (i) shows linear scans of a solution containing 0.5 mM **1'**$^+$ complex in 0.1 M TBAHFP, 40 mM MOPS, 50mM $NaNO_2$. (ii)Shows a scan after the electrode was removed, rinsed with clean solvent and placed in a fresh solution containing no Ni complex.

Computational analysis to support the proposed mechanism.

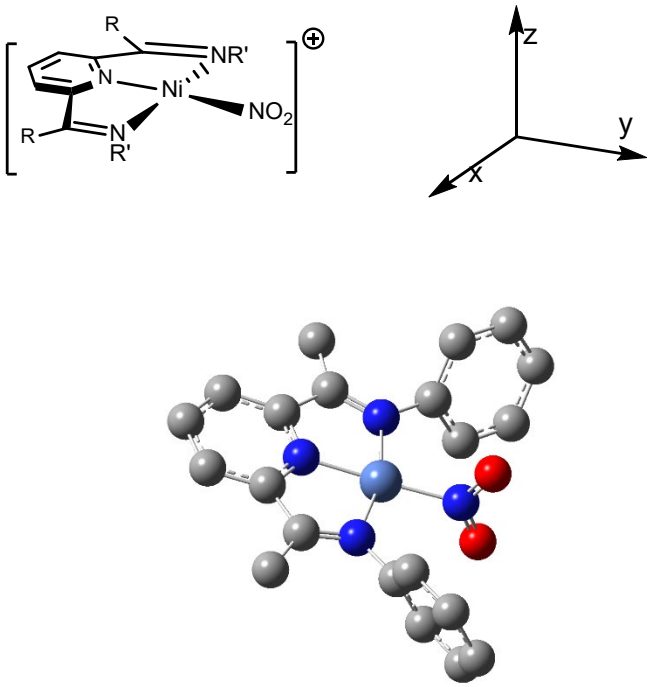

Figure S21. DFT optimized structure of $[Ni(\kappa^3\text{-}2,6\text{-}\{Ph_2PNH\}_2NC_5H_3)NO_2]^+$ (**1'NO$_2^+$**) using the B3LYP functional and def2TZVP basis set in water (IEFPCM). Hydrogen atoms omitted for clarity. Frequency analysis confirmed that the optimized structure was a minimum with no imaginary frequencies.

Table S5. Summary of Ni-centered bonding for $[Ni(\kappa^3\text{-}2,6\text{-}\{Ph_2PNH\}_2NC_5H_3)NO_2]^+$ (**1'NO$_2^+$**). Values for bond length, overlap populations and Mayer bond order indices are from the B3LYP/def2TZVP/IEFPCM (water) optimization.

Bond	Length(Å)	Overlap Population	Mayer Bond order
Ni-N_{py}	1.866	0.153	0.594
Ni-N_{imine}	1.975	0.258	0.628
Ni-N_{imine}	1.975	0.258	0.628
Ni-$N_{nitrite}$	1.856	0.238	0.658
N-O	1.219	0.288	1.530
N-O	1.221	0.306	1.541

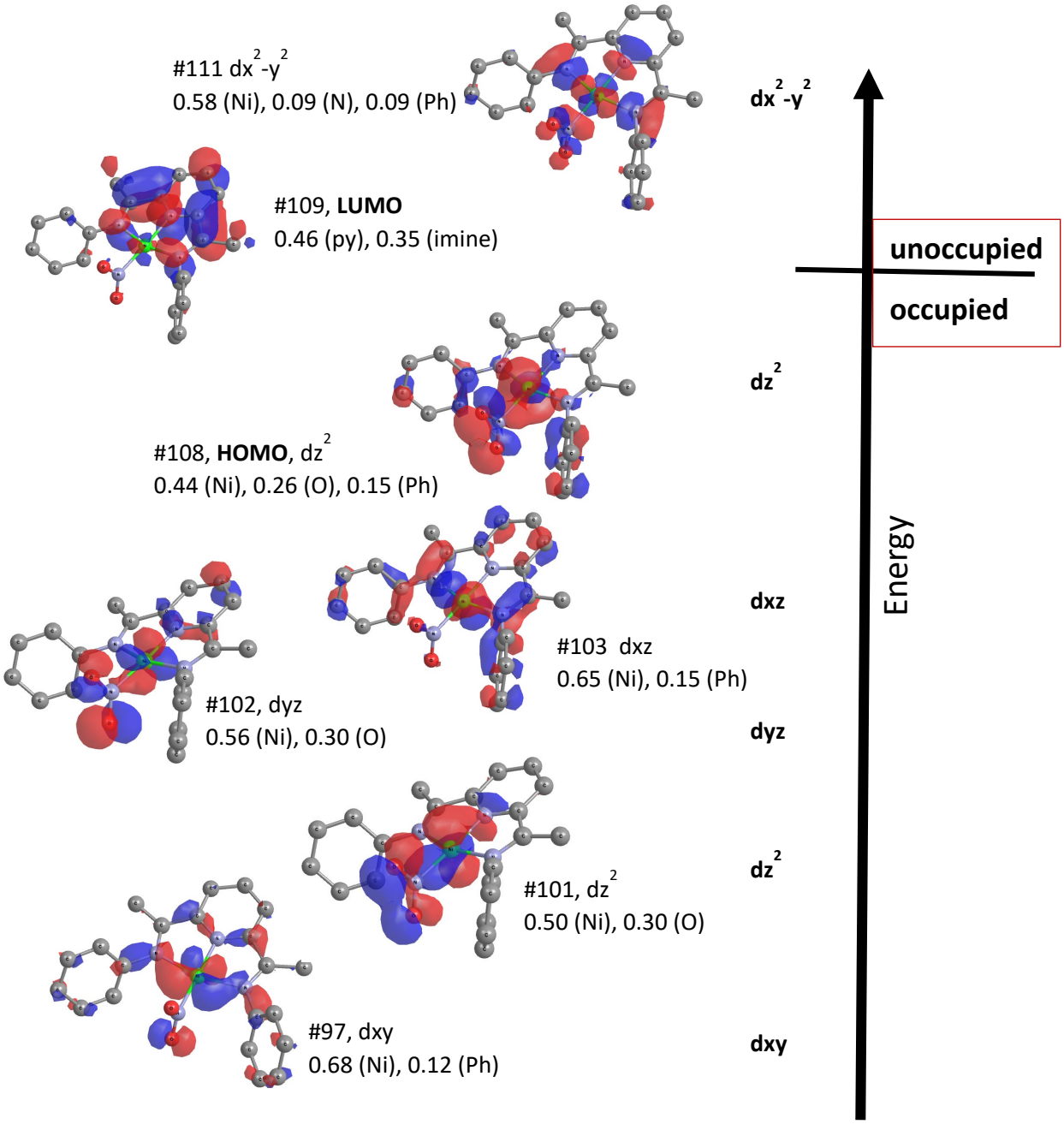

Figure S22. Selected, Ni-centered molecular orbitals obtained from the computational optimization of $[Ni(\kappa^3\text{-}2,6\text{-}\{Ph_2PNH\}_2NC_5H_3)NO_2]^+$ (**1'NO$_2^+$**) using the B3LYP functional, def2TZVP basis set and IEFPCM model for solvation in acetonitrile. Hydrogen atoms omitted for clarity. Major fragment orbital contributions were obtained from the Chemissian program.

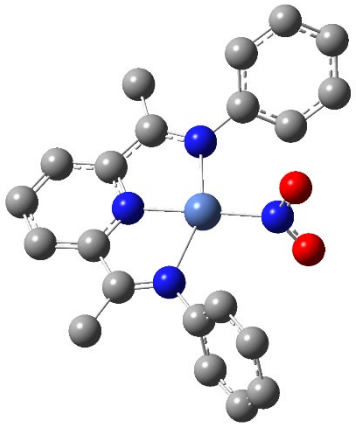

Figure S23. DFT optimized structure of [Ni(κ^3-2,6-{Ph_2PNH}$_2$$NC_5H_3$)$NO_2$]$^-$ (**Ni(NO_2)$^-$**) in the triplet state using the B3LYP functional and def2TZVP basis set in water (IEFPCM). Hydrogen atoms omitted for clarity. Frequency analysis confirmed that the optimized structure was a minimum with no imaginary frequencies.

Table S6. Summary of Ni-centered bonding for [Ni(κ^3-2,6-{Ph_2PNH}$_2$$NC_5H_3$)$NO_2$]$^-$ (**Ni(NO_2)$^-$**) in triplet state. Values for bond length, overlap populations and Mayer bond order indices are from the B3LYP/def2TZVP/IEFPCM (water) optimization.

Bond	Length(Å)	Overlap Population	Mayer Bond order
Ni-N_{py}	1.937	0.164	0.543
Ni-N_{im}	2.141	0.170	0.409
Ni-N_{im}	2.208	0.142	0.322
Ni-$N_{nitrite}$	1.974	0.249	0.557
N-O	1.250	0.213	1.452
N-O	1.250	0.215	1.455

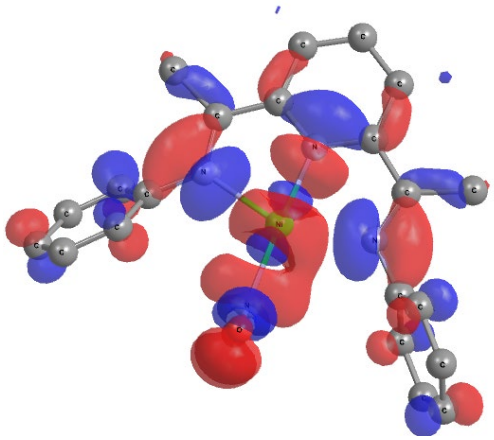

Figure S24. SOMO (MO 109) for [Ni(κ^3-2,6-{Ph_2PNH}$_2$$NC_5H_3$)$NO_2$]$^-$ (**Ni(NO_2)$^-$**) in the triplet state using the B3LYP functional and def2TZVP basis set in water (IEFPCM). Hydrogen atoms omitted for clarity. The major orbital fragment allocation: 0.49 (Ni), 0.17 (imine), 0.16 (NO_2), 0.11 (py), and 0.07 (Ph).

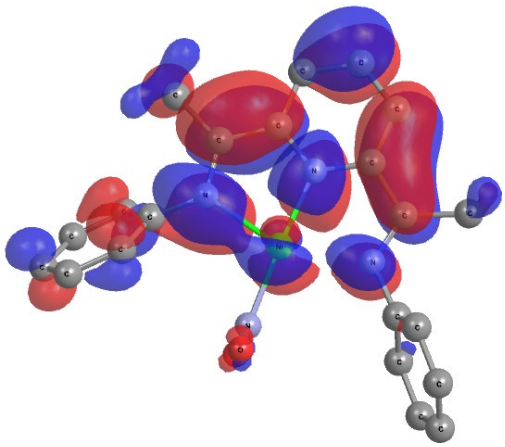

Figure S25. SOMO (MO 110) for [Ni(κ^3-2,6-{Ph_2PNH}$_2$$NC_5H_3$)$NO_2$]$^-$ (**Ni(NO_2)$^-$**) in the triplet state using the B3LYP functional and def2TZVP basis set in water (IEFPCM). Hydrogen atoms omitted for clarity. The major orbital fragment allocation: 0.46 (py), 0.40 (imine), 0.07 (Ph), 0.06 (Ni).

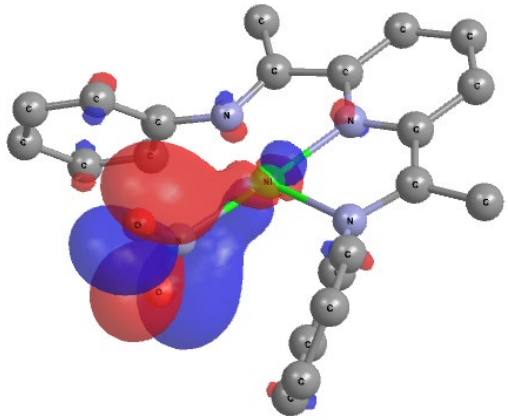

Figure S26. Molecular orbital 101 for [Ni(κ^3-2,6-{Ph_2PNH}$_2$$NC_5H_3$)$NO_2$]$^-$ (**Ni(NO_2)$^-$**) in the triplet state using the B3LYP functional and def2TZVP basis set in water (IEFPCM). Hydrogen atoms omitted for clarity. The major orbital fragment allocation: 0.85 (NO_2).

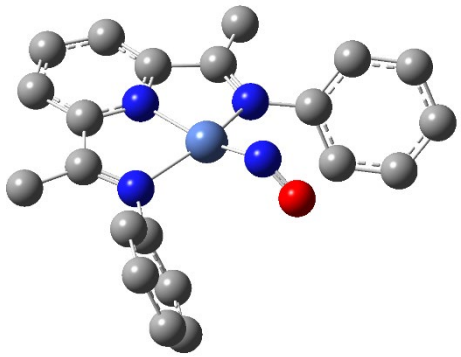

Figure S27. DFT optimized structure of [Ni(κ^3-2,6-{Ph_2PNH}$_2$$NC_5H_3$)NO]$^+$ (**Ni(NO)$^+$**) using the B3LYP functional and def2TZVP basis set in water (IEFPCM). Hydrogen atoms omitted for clarity. Frequency analysis confirmed that the optimized structure was a minimum with no imaginary frequencies.

Table S7. Summary of Ni-centered bonding for [Ni(κ^3-2,6-{Ph_2PNH}$_2$$NC_5H_3$)NO]$^+$ (**Ni(NO)$^+$**). Values for bond length, overlap populations and Mayer bond order indices are from the B3LYP/def2TZVP/IEFPCM (water) optimization.

Bond	Length(Å)	Overlap Population	Mayer Bond order
Ni-N_{py}	1.941	0.194	0.497
Ni-N_{imine}	2.038	0.200	0.505
Ni-N_{imine}	2.040	0.199	0.502
Ni-$N_{nitrosyl}$	1.694	0.269	1.221
N-O	1.173	0.250	1.720

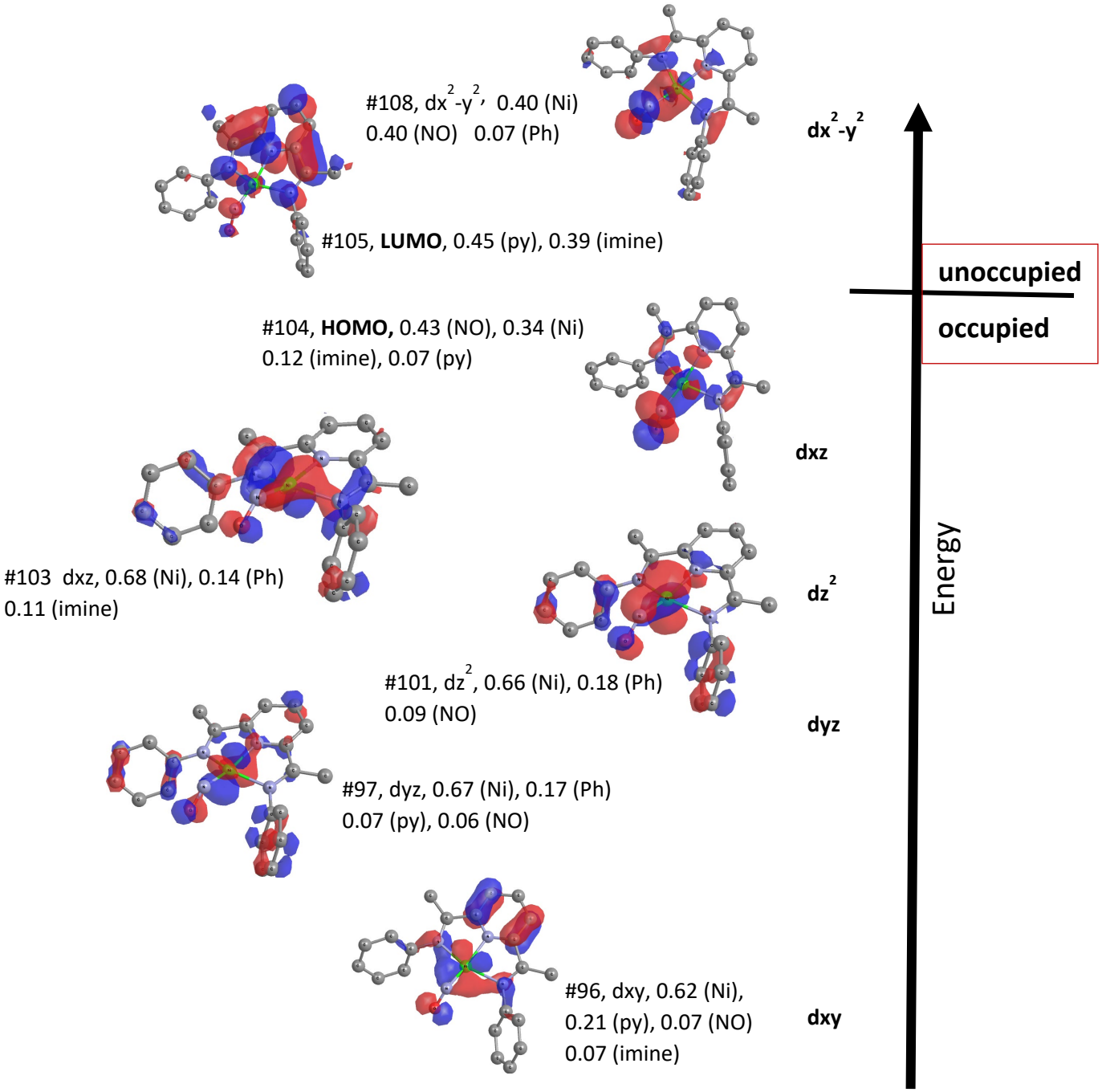

Figure S28. Selected, Ni-centered molecular orbitals obtained from the computational optimization of $[Ni(\kappa^3\text{-}2,6\text{-}\{Ph_2PNH\}_2NC_5H_3)NO]^+$ (**Ni(NO)$^+$**) using the B3LYP functional, def2TZVP basis set and IEFPCM model for solvation in water. Hydrogen atoms have been omitted for clarity. Major fragment orbital contributions were obtained from the Chemissian program.

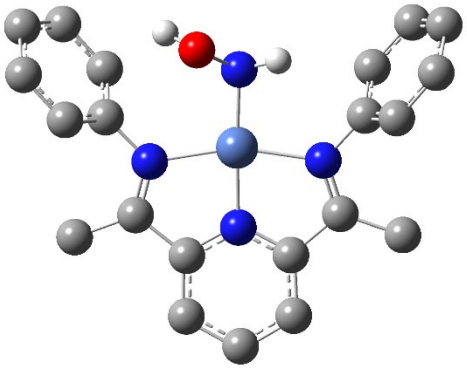

Figure S29. DFT optimized structure of [Ni(κ^3-2,6-{Ph_2PNH}$_2$$NC_5H_3$)(N(H)OH)]$^+$ (**Ni(NHOH)$^+$**) using the B3LYP functional and def2TZVP basis set in water (IEFPCM). Hydrogen atoms on carbon omitted for clarity. Frequency analysis confirmed that the optimized structure was a minimum with no imaginary frequencies.

Table S8. Summary of Ni-centered bonding for [Ni(κ^3-2,6-{Ph_2PNH}$_2$$NC_5H_3$)(N(H)OH)]$^+$ (**Ni(NHOH)$^+$**). Values for bond length, overlap populations and Mayer bond order indices are from the B3LYP/def2TZVP/IEFPCM (water) optimization.

Bond	Length(Å)	Overlap Population	Mayer Bond order
Ni-N_{py}	1.874	0.187	0.597
Ni-N_{imine}	2.007	0.258	0.591
Ni-N_{imine}	1.969	0.263	0.627
Ni-N	1.832	0.255	0.882
N-O	1.424	0.064	0.868

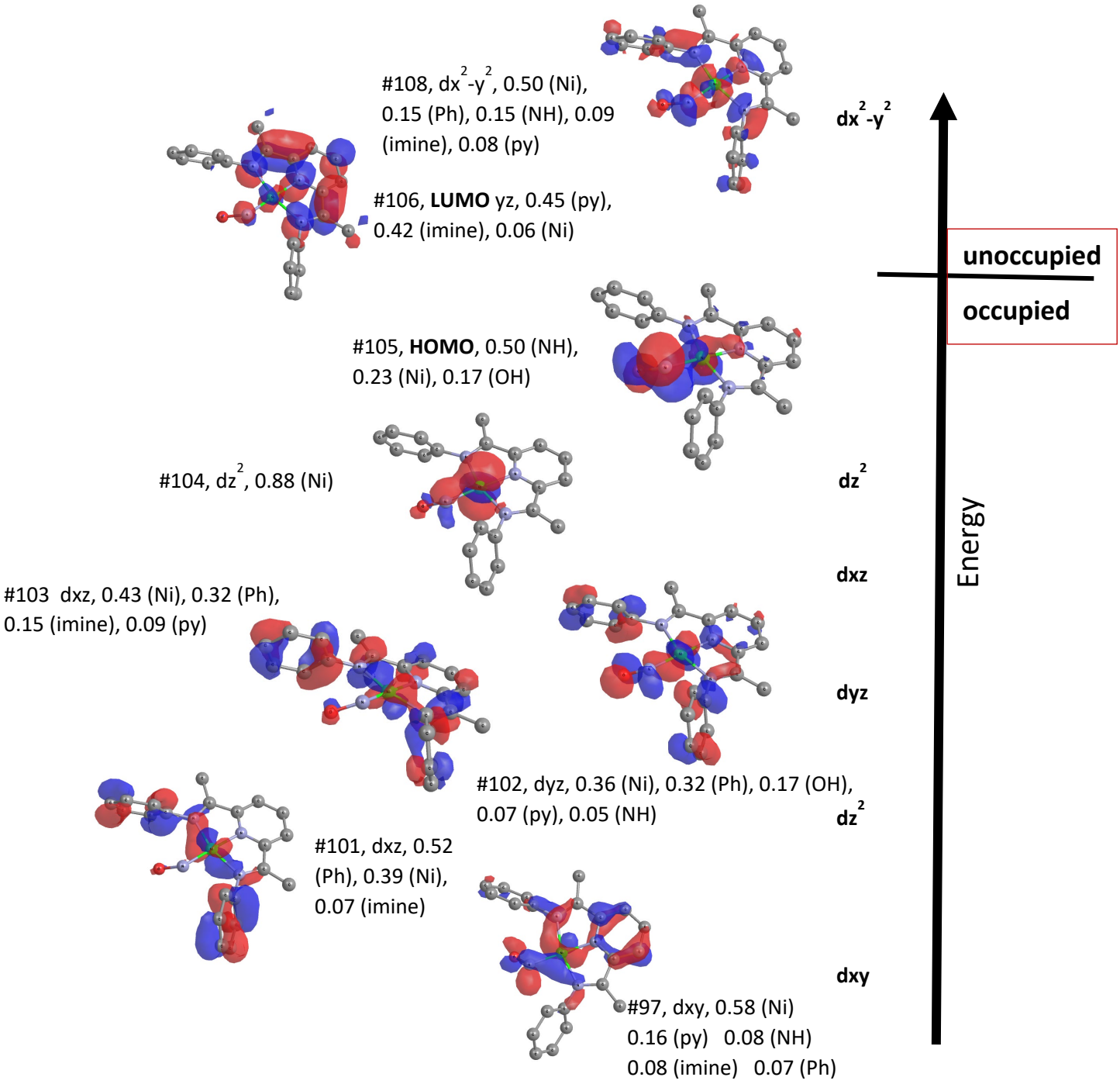

Figure S30. Selected, Ni-centered molecular orbitals obtained from the computational optimization of $[Ni(\kappa^3\text{-}2,6\text{-}\{Ph_2PNH\}_2NC_5H_3)(N(H)OH)]^+$ (**Ni(NHOH)**$^+$) using the B3LYP functional, def2TZVP basis set and IEFPCM model for solvation in water. Hydrogens atoms omitted for clarity. Major fragment orbital contributions were obtained from the Chemissian program.

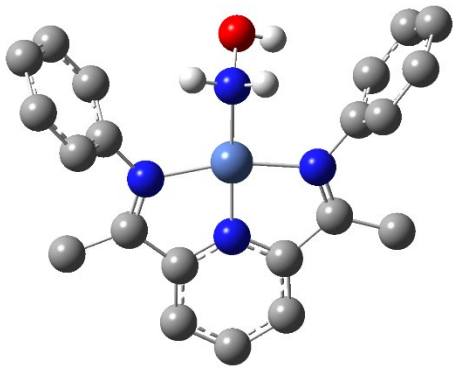

Figure S31. DFT optimized structure of $[Ni(\kappa^3\text{-}2,6\text{-}\{Ph_2PNH\}_2NC_5H_3)(NH_2OH)]^{2+}$ (**$Ni(NH_2OH)^{2+}$**) using the B3LYP functional and def2TZVP basis set in water (IEFPCM). Hydrogen atoms on carbon omitted for clarity. Frequency analysis confirmed that the optimized structure was a minimum with no imaginary frequencies.

Table S9. Summary of Ni-centered bonding for $[Ni(\kappa^3\text{-}2,6\text{-}\{Ph_2PNH\}_2NC_5H_3)(NH_2OH)]^{2+}$ (**$Ni(NH_2OH)^{2+}$**). Values for bond length, overlap populations and Mayer bond order indices are from the B3LYP/def2TZVP/IEFPCM (water) optimization.

Bond	Length(Å)	Overlap Population	Mayer Bond order
$Ni\text{-}N_{py}$	1.843	0.200	0.682
$Ni\text{-}N_{imine}$	1.955	0.267	0.655
$Ni\text{-}N_{imine}$	1.960	0.270	0.665
Ni-N	1.950	0.189	0.572
N-O	1.415	0.109	0.928

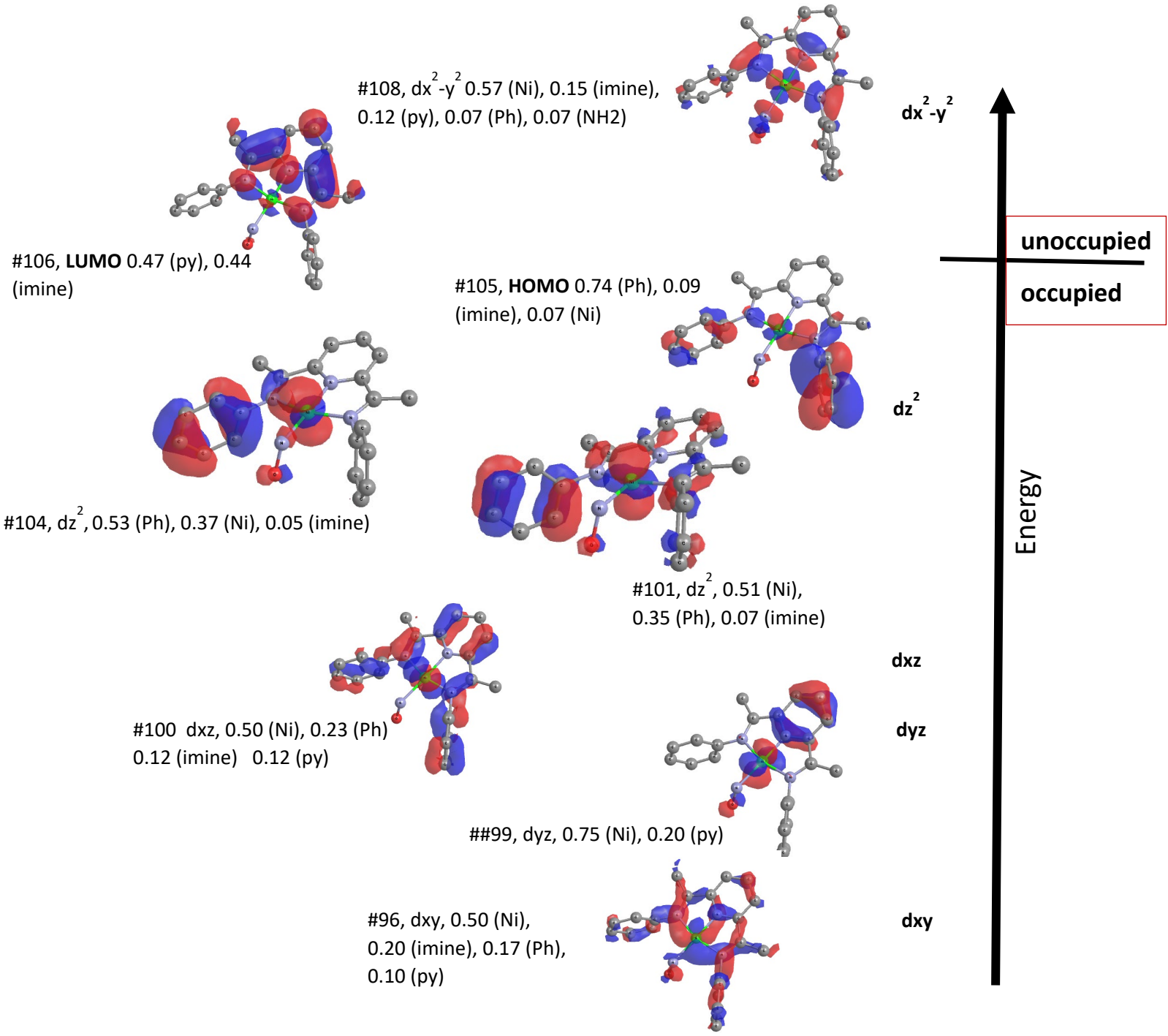

Figure S32. Selected, Ni-centered molecular orbitals obtained from the computational optimization of $[Ni(\kappa^3\text{-}2,6\text{-}\{Ph_2PNH\}_2NC_5H_3)(NH_2OH)]^{2+}$ (**$Ni(NH_2OH)^{2+}$**) using the B3LYP functional, def2TZVP basis set and IEFPCM model for solvation in water. Hydrogen atoms omitted for clarity. Major fragment orbital contributions were obtained from the Chemissian program.

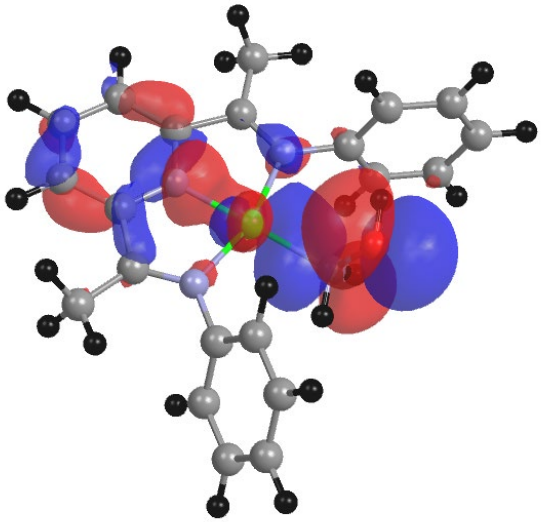

Figure S33. Molecular orbital #97 for $[Ni(\kappa^3\text{-}2,6\text{-}\{Ph_2PNH\}_2NC_5H_3)(NH_2OH)]^{2+}$ (**$Ni(NH_2OH)^{2+}$**) using the B3LYP functional and def2TZVP basis set in water (IEFPCM). The major orbital fragment allocation: 0.56 (OH), 0.19 (NH2), 0.11 (Ni), 0.09 (py).

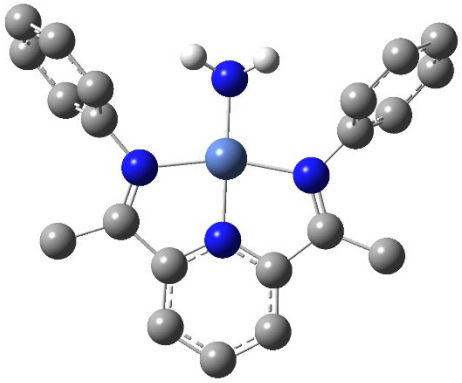

Figure S34. DFT optimized structure of $[Ni(\kappa^3\text{-}2,6\text{-}\{Ph_2PNH\}_2NC_5H_3)(NH_2)]^+$ (**$Ni(NH_2)^+$**) using the B3LYP functional and def2TZVP basis set in water (IEFPCM). Hydrogen atoms on carbon omitted for clarity. Frequency analysis confirmed that the optimized structure was a minimum with no imaginary frequencies.

Table S10. Summary of Ni-centered bonding for $[Ni(\kappa^3\text{-}2,6\text{-}\{Ph_2PNH\}_2NC_5H_3)(NH_2)]^+$ (**$Ni(NH_2)^+$**). Values for bond length, overlap populations and Mayer bond order indices are from the B3LYP/def2TZVP/IEFPCM (water) optimization.

Bond	Length(Å)	Overlap Population	Mayer Bond order
$Ni\text{-}N_{py}$	1.846	0.175	0.614
$Ni\text{-}N_{imine}$	1.961	0.258	0.649
$Ni\text{-}N_{imine}$	1.961	0.258	0.649
$Ni\text{-}N_{amido}$	1.809	0.259	0.860

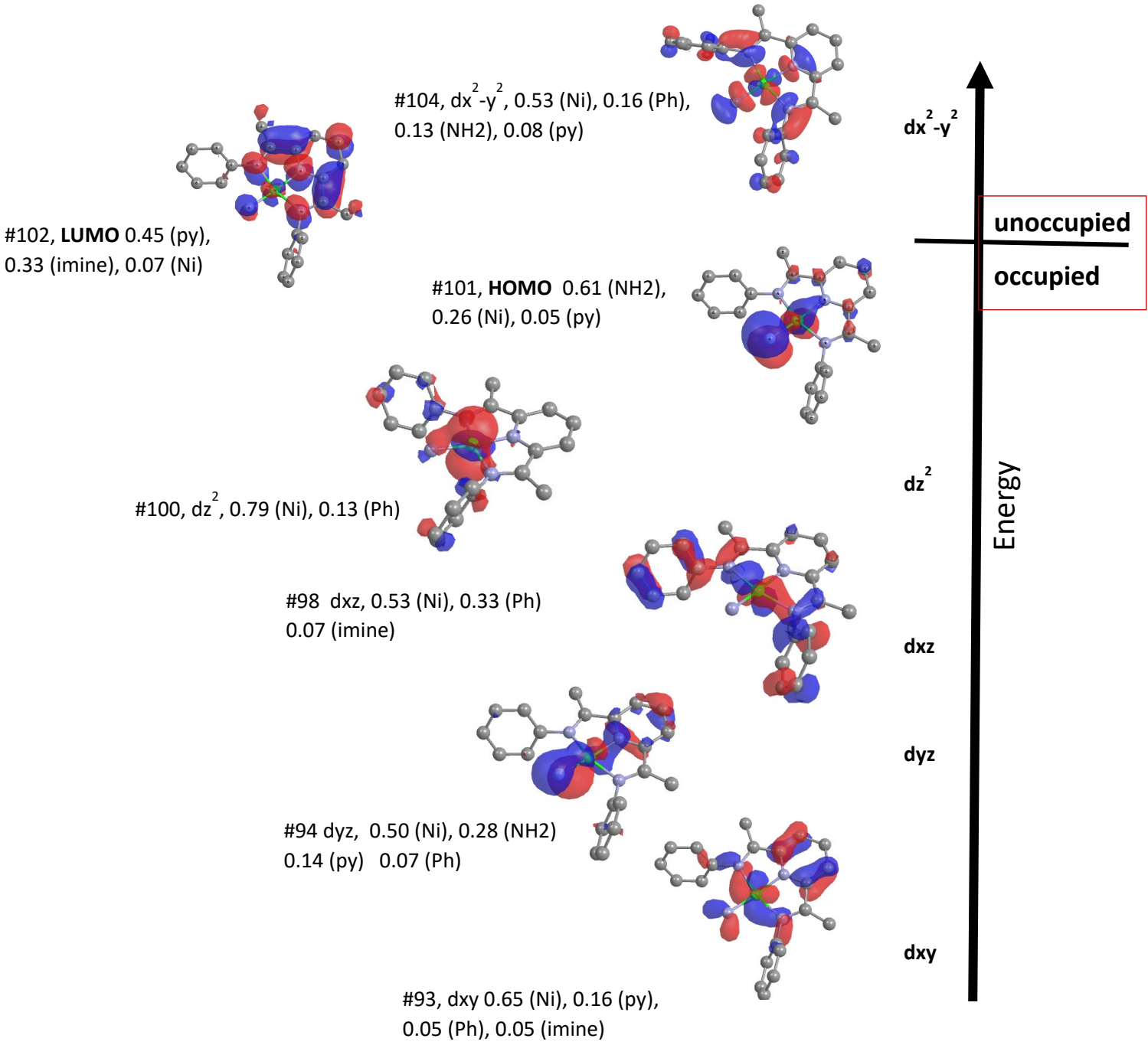

Figure S35. Selected, Ni-centered molecular orbitals obtained from the computational optimization of $[Ni(\kappa^3\text{-}2,6\text{-}\{Ph_2PNH\}_2NC_5H_3)(NH_2)]^+$ (**Ni(NH$_2$)$^+$**) using the B3LYP functional, def2TZVP basis set and IEFPCM model for solvation in water. Hydrogen atoms omitted for clarity. Major fragment orbital contributions were obtained from the Chemissian program.

Table S11. Summary of computed thermochemistry for complexes in the proposed nitrite reduction mechanism.

Compound	Sum of electronic and thermal Enthalpies (a.u.)	Sum of electronic and thermal Free Energies (a.u.)
1'$(NO_2)^+$	-2687.846113	-2687.928049
Ni$(NO_2)^-$ Singlet Triplet	-2689.691655 -2689.69424	-2689.773557 -2689.782047
Ni$(NO)^+$	-2612.762566	-2612.843527
Ni$(NHOH)^+$	-2613.946868	-2614.027187
Ni$(NH_2OH)^{2+}$	-2614.404165	-2614.485435
Ni$(NH_2)^+$	-2539.242994	-2539.40815

References

(1) Norouziyanlakvan, S.; Ferguson, J.; Richeson, D. Electrocatalytic Hydrogen Production from Neutral Water Using an Aqueous Ni(Ii) Pincer Complex. *Catal. Sci. Technol.* **2022**, *12* (24), 7494–7500.

(2) APEX Softward Suite v 2010 Bruker AXS Inc. Madison Wisconsin USA. APEX Softward Suite v 2010. Bruker AXS Inc.: Madison, Wisconsin 2010.

(3) Blessing, R. H. An Empirical Correction for Absorption Anisotropy. *Acta Crystallogr. Sect. A* **1995**, 33–38.

(4) Sheldrick, G. M. A Short History of SHELX. *Acta Crystallogr. Sect. A* **2008**, 112–122.

(5) Hubschle, Christian, B.; Sheldrick, G. M.; Dittrich, B. ShelXle: A Qt Graphical User Interface for SHELXL. *Journal of Applied Crystallography*. 2011, pp 1281–1284.

(6) Stroka, J. R.; Kandemir, B.; Matson, E. M.; Bren, K. L. Electrocatalytic Multielectron Nitrite Reduction in Water by an Iron Complex. *ACS Catal.* **2020**, *10* (23), 13968–13972.

(7) Weatherburn, M. W. Phenol-Hypochlorite Reaction for Determination of Ammonia. *Anal. Chem.* **1967**, *39* (8), 971–974.

(8) Hu, B.; Tian, X. L.; Shi, W. N.; Zhao, J. Q.; Wu, P.; Mei, S. T. Spectrophotometric Determination of Hydroxylamine in Biological Wastewater Treatment Processes. *Int. J. Environ. Sci. Technol.* **2018**, *15* (2), 323–332.

(9) Frisch, M. J.; Trucks, G. W.; Schlegel, H. B.; Scuseria, G. E.; Robb, M. A.; Cheeseman, J. R.; Scalmani, G.; Barone, V.; Petersson, G. A.; Nakatsuji, H.; et al. Gaussian 09 (Revision A.02). Gaussian Inc.: Wallingford, CT 2016.

(10) Costentin, C.; Robert, M.; Savéant, J.-M. Catalysis of the Electrochemical Reduction of Carbon Dioxide. *Chem. Soc. Rev.* **2013**, *42* (6), 2423–2436.

(11) Costentin, C.; Drouet, S.; Robert, M.; Savéant, J. M. Turnover Numbers, Turnover Frequencies, and Overpotential in Molecular Catalysis of Electrochemical Reactions. Cyclic Voltammetry and Preparative-Scale Electrolysis. *J. Am. Chem. Soc.* **2012**, *134* (27), 11235–11242.

(12) Rountree, E. S.; Dempsey, J. L. Potential-Dependent Electrocatalytic Pathways: Controlling Reactivity with PKa for Mechanistic Investigation of a Nickel-Based Hydrogen Evolution Catalyst. *J. Am. Chem. Soc.* **2015**, *137* (41), 13371–13380.

(13) Rountree, E. S.; Mccarthy, B. D.; Eisenhart, T. T.; Dempsey, J. L. Evaluation of Homogeneous Electrocatalysts by Cyclic Voltammetry. *Inorg. Chem.* **2014**, *53*, 9983–10002.